Impact of Cesium/Rubidium Incorporation on the Photophysics of Multiple-Cation Lead Halide Perovskites

Impact of Cesium/Rubidium Incorporation on the Photophysics of Multiple-Cation Lead Halide Perovskites

Yajun Gao,[+] Kai Wang[+], Mingcong Wang, Jafar I. Khan, Ahmed Balawi, Wenzhu Liu, Stefaan De Wolf, Frédéric Laquai**

King Abdullah University of Science and Technology (KAUST), KAUST Solar Center (KSC), Physical Sciences and Engineering Division (PSE), Material Science and Engineering Program (MSE), Thuwal 23955-6900, Kingdom of Saudi Arabia

Corresponding authors: yajun.gao@kaust.edu.sa; frederic.laquai@kaust.edu.sa

Keywords: lead halide perovskites, photovoltaics, ultrafast spectroscopy, carrier dynamics, carrier cooling

Abstract

Incorporating cesium (Cs) or rubidium (Rb) cations into multiple-cation lead mixed-halide perovskites ($FA_{0.83}MA_{0.17}Pb(I_{0.83}Br_{0.17})_3$) increases their photovoltaic performance. In this study, the fundamental photophysics of perovskites are investigated by steady-state and transient optical spectroscopy and the reasons for the performance increase are revealed. Cs/Rb-cation incorporation slightly increases the bandgap, while exciton binding energies remain in the range of a few meV. Urbach energies are reduced, suggesting improved perovskite microstructure upon Cs/Rb incorporation. Carrier density-induced broadening of the photo-bleaching following the Burstein-Moss model is observed, and the effective carrier masses are determined to be a few tenths of the electron rest mass. From fits of the high-energy tail of the perovskite's photo bleach to Boltzmann's distribution, sub-picosecond hot carrier cooling is revealed, implying strong carrier-phonon coupling. Importantly, the charge carrier recombination dynamics indicate that Cs/Rb-incorporation reduces both the first-order (trap-assisted) and the second-order (radiative) recombination, which appears to be the main reason for the observed performance increase upon Cs/Rb-cation incorporation. Overall, this work presents a

This article has been accepted for publication and undergone full peer review but has not been through the copyediting, typesetting, pagination and proofreading process, which may lead to differences between this version and the Version of Record. Please cite this article as doi: 10.1002/solr.202000072.

detailed study of the photophysics of multiple-cation mixed halide lead perovskites and develops a concise picture of the impact of cesium/rubidium incorporation on the photophysics and device performance.

1. Introduction

In less than a decade, solar cells based on metal halide perovskites have reached power conversion efficiencies (PCEs) above 25%.[1-5] Flexible solar cells,[6-7] tandem devices,[8-9] and large-area printed solar cells [10] have been demonstrated; however, the PCEs of all these devices can be further improved towards to the Shockley-Queisser limit.[11] Apart from device engineering, the photovoltaic performance is strongly dictated by the electronic quality of the lead-halide perovskite absorber, which benefits from incorporating different monovalent cations (here Cs^+ and Rb^+) into its lattice.[12-14] This leads not only to increased performance, but also to better thermal stability and improved device reproducibility.[15-16] However, the precise reasons for these improvements are still unclear and fundamental studies of the effect of Cs/Rb-ion incorporation are scarce. In fact, most work to date has mainly focused on how the incorporation contributes to the stability of the perovskite phase and changes the perovskite's entropy,[12, 14, 17] whereas only few investigations have addressed the impact of incorporation of monovalent cations on the photophysics of lead-halide perovskites.[18-19]

Several groups have presented in-depth studies of the photophysical processes in metal halide perovskites featuring organic cations (mainly methylammonium (MA) cation: $CH_3NH_3^+$) by steady-state optical and time-resolved spectroscopy. For instance, the Herz group investigated charge recombination and carrier mobility in $CH_3NH_3PbI_3$ and $CH_3NH_3PbI_{3-x}Cl_x$ films using transient THz spectroscopy.[20-21] The Beard group determined the band gap and excitonic binding energy of $CH_3NH_3PbI_3$ films and single crystals by applying the Elliott model on the steady-state absorption spectra; furthermore, they studied hot-carrier cooling and surface recombination, limiting device performance.[22-23] De Wolf *et al.* used photothermal deflection spectroscopy (PDS), Fourier-transform photocurrent spectroscopy (FTPS) and photoluminescence (PL) to investigate sub-band gap absorption of CH_3NH_3PbI3 films.[24-25] Snaith *et al.* demonstrated improved microstructure upon thermal treatment revealed by PDS.[26] Using time-resolved photoluminescence (TRPL) spectroscopy, Sum *et al*. determined the carrier diffusion length of $CH_3NH_3PbI_3$ films by comparing the carrier

dynamics and lifetimes in the presence of different charge extraction layers.[27] Moreover, transient absorption (TA) spectroscopy has been used by the Kamat and Friend groups to determine the effective carrier masses for $CH_3NH_3PbI_3$ films by analyzing the carrier density-induced broadening of the ground-state photo bleach signal in the framework of the Burstein-Moss model.[28-29]

Whereas the aforementioned works have focused on $CH_3NH_3PbI_3$ and $CH_3NH_3PbI_{3-x}Cl_x$ films, in the present study we use steady-state and time-resolved spectroscopic techniques to reveal the impact of Cs/Rb-cation incorporation on the fundamental photophysics of multiple-cation lead mixed halide perovskites, specifically the previously-reported high-efficiency formamidinium (FA) cation-containing $FA_{0.83}MA_{0.17}Pb(I_{0.83}Br_{0.17})_3$ perovskite[13-14, 30]. Firstly, by analyzing the absorption spectrum close to the band-edge in the framework of the Elliott model, we show that Cs/Rb incorporation slightly increases the optical bandgap, whereas the exciton binding energies remain in the range of a few meV. Secondly, we measured sub-bandgap absorption by PDS, from which we found that Cs/Rb incorporation desirably reduces the Urbach energy, indicating improved microstructure. Thirdly, we studied charge recombination by transient absorption (TA) pump-probe spectroscopy and analyzed the density-dependent decay dynamics using a general recombination model, which includes first-, second-, and third-order recombination processes, corresponding to defect-assisted, radiative and Auger recombination, respectively. Here, we find that the first-order recombination rate is on the order of 10^7 s^{-1} and that Cs/Rb-cation incorporation reduces this rate. The second-order recombination rate of 10^{-11} cm^3s^{-1} implies that reduced Langevin recombination occurs in these perovskite films. The third-order recombination rate is on the order of 10^{-29}~10^{-28} cm^6s^{-1} and shows that Auger-type non-radiative recombination losses are negligible under the operation condition of solar cells.

Furthermore, we analyzed the carrier density-induced broadening of the photo-bleaching signal in the framework of the Burstein-Moss model and thereby estimated the effective carrier mass to be a few tenths of the electron rest mass, explaining the exceptional charge carrier mobilities of these perovskite films. Lastly, we explored hot-carrier cooling dynamics by assuming that hot carriers reach a quasi-equilibrium state and that

their distribution follows Maxwell-Boltzmann statistics. We observe sub-picosecond cooling times, indicating strong phonon-charge coupling. Interestingly, Cs/Rb-cation incorporation does not alter the cooling dynamics.

2. Results and discussion

2.1 Photovoltaic device performance

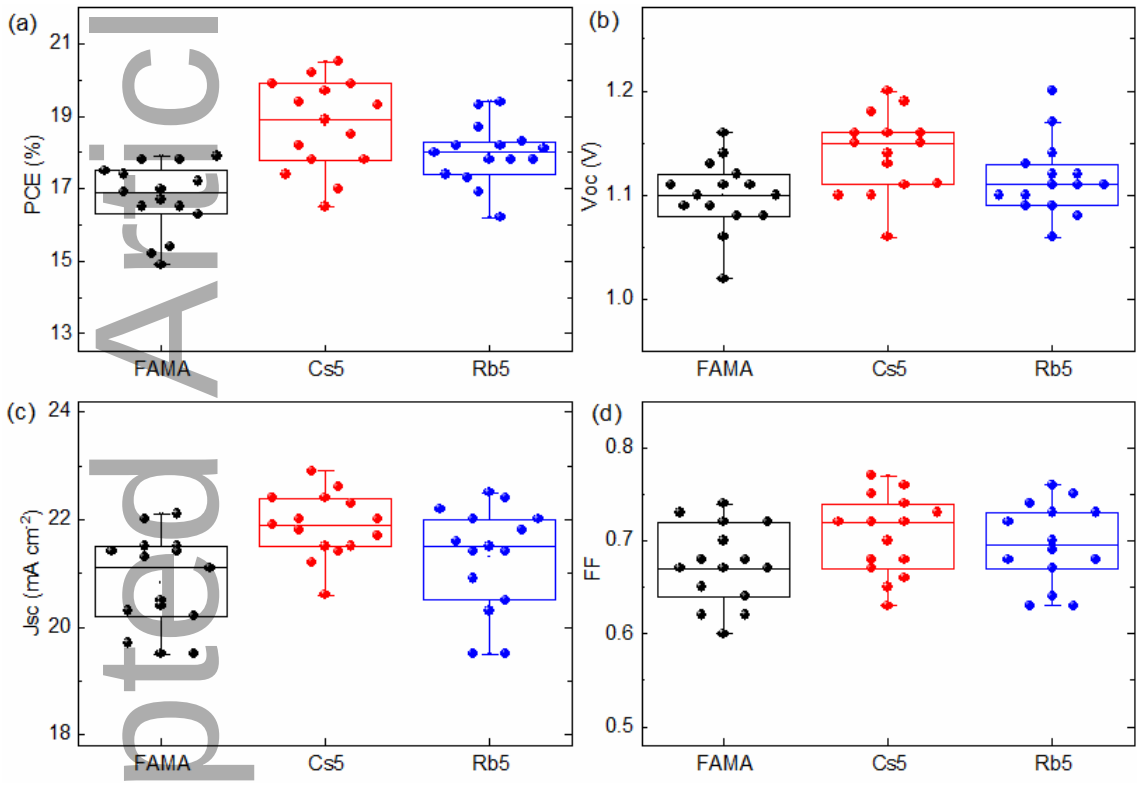

Figure 1. (a-d) Box chart representation of perovskite-based solar cell performance parameters under simulated AM 1.5G sunlight, where FAMA represents the reference perovskite $FA_{0.83}MA_{0.17}Pb(I_{0.83}Br_{0.17})_3$, Cs5 and Rb5 represent the Cs-incorporated $Cs_{0.05}[FA_{0.83}MA_{0.17}]_{0.95}Pb(I_{0.83}Br_{0.17})_3$ and Rb-incorporated $Rb_{0.05}[FA_{0.83}MA_{0.17}]_{0.95}Pb(I_{0.83}Br_{0.17})_3$ perovskites, respectively. Data shown for 15 cells of each perovskite.

To investigate the impact of Cs/Rb-cation incorporation on the photovoltaic performance, planar perovskite solar cells (PSCs) of the following structure were prepared: ITO/SnO_2/perovskite/2,2′,7,7′-tetrakis-(N,N-di-pmethoxyphenyl-amine)-9,9′-spirobifluorene (spiro-OMeTAD)/Au. As reference sample the multi-cation lead halide perovskite $FA_{0.83}MA_{0.17}Pb(I_{0.83}Br_{0.17})_3$ was chosen, whereas the Cs- and Rb-incorporated perovskites had the compositions $Cs_{0.05}[FA_{0.83}MA_{0.17}]_{0.95}Pb(I_{0.83}Br_{0.17})_3$ and $Rb_{0.05}[FA_{0.83}MA_{0.17}]_{0.95}Pb(I_{0.83}Br_{0.17})_3$, respectively. The perovskites were synthesized according to protocols outlined earlier by Saliba *et al.*[13, 30] Henceforth, the perovskites are denoted as FAMA, Cs5, and Rb5, respectively. **Figure 1** presents device statistics for 15 cells of each perovskite material under simulated AM

1.5G sunlight. Both Cs- and Rb-cation incorporation improved the PCE values compared to the reference perovskite FAMA. The performance increase is a consequence of improved figures-of-merit, namely open-circuit voltage (Voc), short-circuit current (Jsc), and fill factor (FF). In detail, in the case of Cs5 solar cells, the average Voc increased from 1.10 V to 1.15 V, Jsc from 21.1 mA cm^{-2} to 21.9 mA cm^{-2}, and the resulting PCE from 17.0 % to 18.9 %. In the case of Rb5 incorporation, Voc increased from 1.10 V to 1.12 V, Jsc from 21.1 mA cm^{-2} to 21.5 mA cm^{-2}, and the PCE increased from 17.0 % to 18.1 %. We note that our results are in line with those of earlier reports.[13, 17-18, 22, 30] In the following, we present and discuss the photophysics of FAMA and reveal how they are affected by Cs/Rb-cation incorporation.

2.2 Steady-state optical absorption spectra

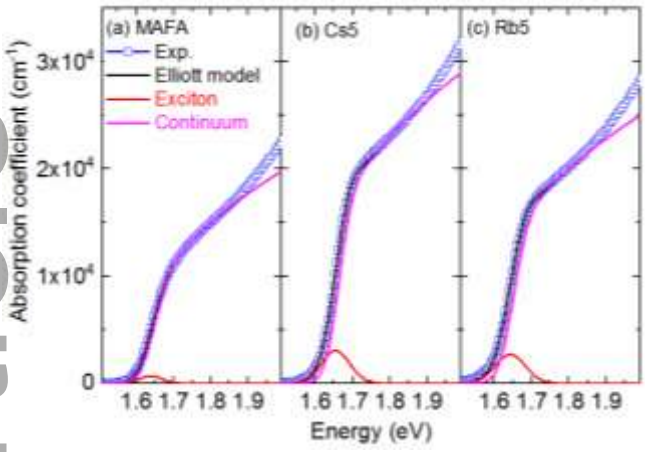

Figure 2. (a) – (c) Band edge absorption spectra of perovskite thin films and fits to the data according to the Elliott model. The absorption coefficient (blue squares) is determined from steady-state UV-Vis absorbance spectra. The black line corresponds to a fit based on the Elliott model, which comprises two contributions: excitonic absorption (red line) and absorption of continuum states (magenta line).

In direct-bandgap semiconductors, the band-edge absorption consists of two contributions: absorption of continuum states and excitonic absorption.[22-23] The former generates free charges, whereas the latter yields (weakly-bound) Wannier-type excitons. To separate these two contributions as well as to determine the bandgap and excitonic binding energy, we used the following modified Elliott model:[22-23, 31]

$$\alpha\,(E) = A * \theta\,(E - Eg) * \left(\frac{\pi\, e^{\pi x}}{\sinh(\pi x)}\right) + A * Rex * \sum_{n=1}^{\infty} \left\{\frac{4\pi}{n^3} * \delta\left[E - Eg - Rexn2,\quad x = RexE - Eg\right.\right. \qquad \textit{Equation 1}$$

Here, the first and second term represent the continuum-states and excitonic contribution, respectively, A is related to the transition matrix element, E the photon energy, E_g the band gap, R_{ex} the exciton binding energy, n the principal quantum number. θ and δ are step and delta functions, respectively. Taking into account inhomogeneous broadening, two Gaussian functions were used to convolve the continuum state and excitonic contributions, respectively. **Figure 2** compares the as-measured steady-state absorption spectra with fits based on the modified Elliott model (see SI for further details). Clearly, the fits reproduce the experimental data, supporting the applicability of the Elliott model to describe the perovskite's absorption spectrum. Accordingly,

we estimated both the bandgap and exciton binding energies from the Elliott model; results summarized in **Table 1**.

Table 1. *Bandgap (Eg) and excitonic binding energy (Rex) of perovskite films investigated in this study.*

Sample	E_g (eV)	R_{ex} (meV)
FAMA	1.650 ± 0.005	3.1 ± 0.9
Cs5	1.677 ± 0.004	8.8 ± 1.4
Rb5	1.670 ± 0.004	10.9 ± 1.4

Compared to the FAMA reference sample, Cs/Rb-cation incorporation slightly increases the perovskite's bandgap. The bandgap increase is consistent with reports published earlier. It can be explained theoretically using first-principle calculations.[19, 32] Briefly, the band-edge states of hybrid metal-halide perovskites are governed by the Pb-6p orbital (contributing to the conduction band minimum) and the hybridized Pb-6s and halide-5p orbitals (contributing to the valence band maximum). Cation substitution in the A-site of the perovskite structure influences the bandgap through the Jahn-Teller effect by changing the volume and orientation of the A-site.[32] Consequently, the smaller-sized Cs/Rb-cation tends to increase the band gap slightly due to octahedral tilting.[33]

The exciton binding energies presented in Table 1 are comparably small in all samples. In fact, we found that Cs/Rb-incorporation increases exciton binding energies to the range of 7.0 ~ 8.3 meV. Both the trend and absolute values are consistent with results reported earlier by Liu *et.al* for Cs-containing perovskites.[19] As the exciton binding energy is significantly below the thermal energy (k_BT, with k_B the Boltzmann constant), photoexcitation likely creates free charges at room temperature.

2.3 Urbach energies

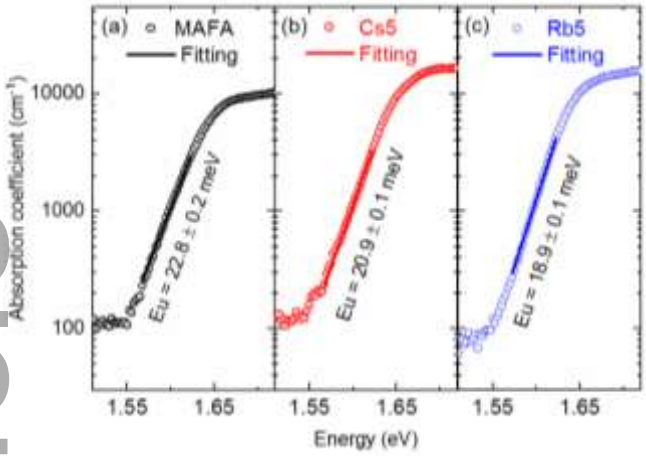

Figure 3. Photothermal deflection spectroscopy (PDS) spectra of perovskite films. The Urbach energy (E_u) is estimated by fitting the absorption tail with a single-exponential funtion. Solid lines are fits to the data.

The sub-bandgap absorption spectra were measured by PDS and they are shown in **Figure** 3. Below the bandgap of the perovskite, we observed the characteristic exponential Urbach tail,[25-26, 34-35] which can be fitted according to:

$$\alpha = A * \exp\left(\frac{E - E_C}{E_u}\right) \qquad \textit{Equation 2}$$

where α is the material's absorption coefficient, E, the photon energy, E_u the Urbach energy, and E_C and A are material constants.[25] We found Urbach energies in the range of 18.2 - 22.8 meV. We note that the spectral resolution of our PDS setup is about 7.0 meV in the spectral region of the perovskite's Urbach absorption. Both the fitting parameters and the width of the incident light spectrum are shown in the supporting information. We note that De Wolf *et al*. have recently demonstrated that the Urbach energy measured by PDS can in absolute terms be overestimated due to the detection limit of PDS.[25] In effect, comparing our results to those published earlier, the Urbach energies extracted here are larger than those of $CH_3NH_3PbI_3$ perovskite films (~15 meV at room temperature) reported by De Wolf *et al*. using Fourier-transform photocurrent spectroscopy (FTPS) and photoluminescence measurements.[24-25] Nevertheless, PDS data can still be used to make relative comparisons, as in Figure 3. Qualitatively, this figure indicates that the Urbach energy is slightly reduced as a result of the Cs/Rb-cation incorporation in the films. Since the Urbach energy reflects the structural disorder,[24-25] its

decrease upon Cs/Rb incorporation can be interpreted as improved structural order of the perovskite films, possibly resulting in less trap states and therefore a reduced first-order (trap-assisted) recombination rate (as will be shown below), leading to improved photovoltaic performance (Figure 1).

2.4 Charge carrier density-dependent recombination dynamics

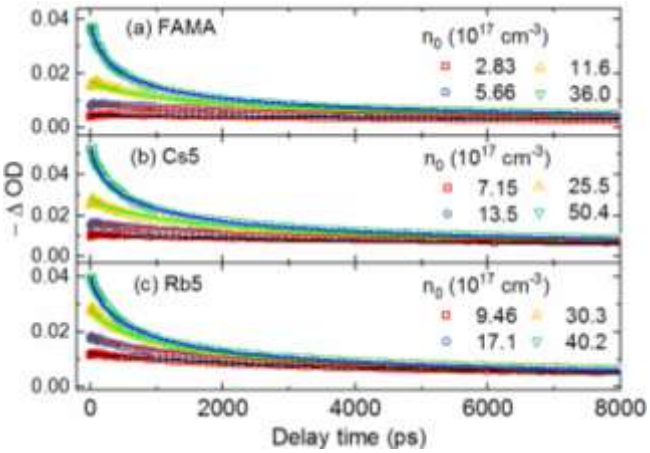

Figure 4. Density-dependent charge carrier recombination monitored at the perovskites' photo-bleach (open symbols). Global fitting (solid lines) based on Equation 3, the general rate equation.

Figure 4 presents the photo bleaching dynamics of the perovskite samples for different excitation fluence, *i.e.*, initial carrier concentration. The corresponding transient absorption spectra are shown in the Supporting Information. Clearly, the recombination of charges is fluence (carrier density) dependent across the fluence range probed here. We parametrized the decay dynamics by globally fitting the density-dependent decays to the general rate equation:[20, 36]

$$\frac{dn(t)}{dt} = -k_1 n(t) - k_2 n(t)^2 - k_3 n(t)^3 \qquad \textit{Equation 3}$$

where k_1, k_2, and k_3 represent the first-, second-, and third-order recombination rate constants, respectively. All fit parameters are listed in **Table 2**. The first-order recombination rate was independently obtained from time-resolved photoluminescence (TRPL) measurements at low fluences (with initial charge density around $9.0 \cdot 10^{16}$ cm^{-3}, shown in the SI) over the time scale of 500 ns to maximally reduce influences from high-order recombinations and to reduce the number of fit parameters required for the general rate equation.[20]

***Table 2**. Fitting parameters obtained by global fits to the fluence dependent perovskites' photo bleaching dynamics using the general rate equation.*

Sample	k_1 (s^{-1})	k_2 (cm^3 s^{-1})	k_3 (cm^6 s^{-1})

FAMA	$(1.19 \pm 0.03) \times 10^{7}$	$(9.61 \pm 1.54) \times 10^{-11}$	$(2.76 \pm 0.16) \times 10^{-28}$
Cs5	$(1.08 \pm 0.03) \times 10^{7}$	$(1.80 \pm 0.77) \times 10^{-11}$	$(1.24 \pm 0.06) \times 10^{-28}$
Rb5	$(1.07 \pm 0.03) \times 10^{7}$	$(5.20 \pm 0.55) \times 10^{-11}$	$(8.45 \pm 0.35) \times 10^{-29}$

The fit parameters show a similar first order recombination rates on the order of 10^7 s^{-1}, indicating carrier lifetimes of up to hundreds of nanoseconds at low fluences, well in line with earlier reports.[20, 36] The first-order recombination has previously been assigned to trap-assisted recombination of charges according to the Shockley-Read-Hall model.[20, 36]] The slightly decreased first-order recombination rate implies that incorporation of Cs/Rb does not create additional recombination centers;[37] in fact, it appears to reduce the trap density.[18] This is in line with the increased photovoltaic performance as shown in Figure 1 and with the lower Urbach energies, as discussed above. Overall, this may result from the improved crystal quality during processing.[15-16] The second-order recombination rate constants, namely k_2, are on the order of 10^{-11} cm^3s^{-1}. It should be noted that the photon reabsorption is not taken into account here, and this may cause underestimation of the second-order recombination.[38] Accordingly, the Langevin ratio can be calculated by:[21]

$$Langevin\ Ratio = \frac{k_2/\mu}{e/\varepsilon_0\varepsilon_r}, \qquad \textit{Equation 4}$$

where k_2 represents the second-order recombination constant, μ the charge mobility, ε_0 the vacuum permittivity, and ε_r the dielectric constant. We note that carrier mobilities for the same Cs/Rb-containing multiple-cation perovskites have been reported in the range of $20 \sim 60$ $cm^2V^{-1}s^{-1}$.[18] The dielectric constant is calculated based on steady-state absorption measurements, and it is coarsely estimated around $6 \sim 7$ at 850 nm (see SI for the spectra of refractive index and relative dielectric constant). This yields a Langevin ratio of 10^{-6}, well in line with the results reported earlier for $CH_3NH_3PbI_{3-x}Cl_x$ perovskite films by Herz *et al.*[20-21] We note that such a low Langevin ratio implies that these perovskite films can simultaneously exhibit high carrier mobility and low recombination rates,[20-21] which is very beneficial for solar cell performance. Table 2 also indicates that the k_2 value is reduced significantly as a result of the Cs/Rb-cation incorporation. This trend is consistent with earlier reports [18] and in line with the photovoltaic performances shown in Figure 1, implying a correlation between the second-order recombination rate and the device performance exists. In contrast to the first-order recombination process, the second-order recombination in direct bandgap semiconductors is radiative and

reflects the intrinsic properties of the material.[36] Therefore, the change in k_2 implies that Cs/Rb-cation incorporation directly affects the semiconductor's band structure. Lastly, the fitting results reveal that the third order recombination constant k_3 (Auger coefficient) is in the range of 10^{-29} ~ 10^{-28} cm^6s^{-1}. This value is comparable to those obtained previously for $CH_3NH_3PbI_3$ and $CH_3NH_3PbI_{3-x}Cl_x$ films,[20-21] but smaller than that of $CH_3NH_3PbBr_3$ films (10^{-27} cm^6 s^{-1}).[39]

2.5 Effective carrier mass

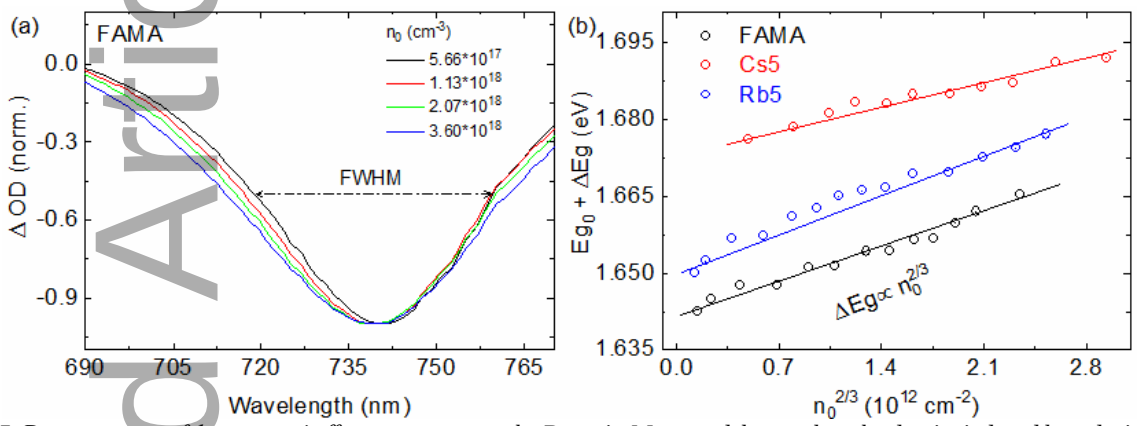

Figure 5. Determination of the carriers' effective mass using the Burstein-Moss model to analyze the density-induced broadening of the photo-bleaching signals. (a) Broadening of the photo-bleaching signal along with the increasing charge density, FWHM: full-width-at-half-maximum. Here, we only show data for the FAMA sample. The spectral broadening of the other perovskite thin films is shown in the Supporting Information. (b) $\Delta Eg \sim n_0^{2/3}$ dependences for each perovskite sample to evaluate the carriers' effective mass. We note that to reduce the influence of hot carrier cooling, the photo-bleaching signals are selected at delay times of 3.0 ps after the hot carrier cooling has concluded.

The transient absorption spectra of perovskites exhibit a characteristic photo-bleaching signal,[27, 29] which spectrally coincides with shoulder in the band-edge absorption of the steady-state absorption spectra (see Supporting Information). Hence, the photo-bleaching signal can be attributed to charges populating band-edge states. Furthermore, the low exciton binding energies imply that the majority of photo-generated states are free charges. Consequently, the Burstein-Moss model can be used to evaluate the effective masses of charge carriers.[28-29] According to this model, a correlation between the shift of the band gap and the density of charges (n) exists, described by Equation 5:

$$\Delta Eg = \left(\frac{3}{2\sqrt{2}}\pi^2\hbar^3\right)^{2/3} * \frac{1}{m^*} * n^{2/3}, \qquad \textit{Equation 5}$$

where $\hbar$ represents the reduced Planck constant, m^* the effective mass, and n the charge density. The derivation of Equation 5 is shown in the supporting information (SI). Equation 5 predicts a linear dependence

of ΔEg on $n^{2/3}$, while the slope is dictated by the reciprocal effective carrier mass. Hence, by plotting ΔEg vs. $n^{2/3}$, as shown in **Figure 5** (b), the effective carrier mass is obtained.

Table 3. *The effective mass (m*) of carriers in perovskites in m_e, the electron rest mass.*

Perovskite	m* (m_e)
FAMA	0.38 ± 0.02
Cs5	0.58 ± 0.04
Rb5	0.35 ± 0.02

Here, the bandgap shift is deduced from the full-width-at-half-maximum (FWHM) of the photo-bleaching signal, as shown in Figure 5 (a). This approach is consistent with that used previously by Kamat *et al.* for $CH_3NH_3PbI_3$ so as to reduce the effect of stimulated emission.[28-29] Here, we select the photo-bleaching signals at 3.0 ps to avoid any distortion caused by hot carriers.[22, 28] Representative spectra indicating the broadening are shown in Figure 5 (b); the $\Delta Eg \sim n^{2/3}$ dependence as well as the fitting results are plotted in Figure 5 (b). Clearly, the model describes the experimental data accurately. Hence, we calculate the effective carrier masses shown in **Table 3**. It is found that the obtained values are consistent with those reported for other hybrid lead halide perovskite materials,[28-29] and the small effective mass explains the high charge carrier mobility.[18] We note the difference in effective mass upon Cs/Rb-incorporation. According to the Burstein-Moss model, the effective mass depends on the curvature of the band structure along all three principal axes of the ellipsoidal energy surface. Therefore, the effective mass difference reflects the variation in band structure as a result of the Cs/Rb-incorporation. This variation is in line with the observed changes of the bandgap (see Table 1) and the second-order recombination coefficient (see Table 2).

2.6 Hot-carrier cooling dynamics

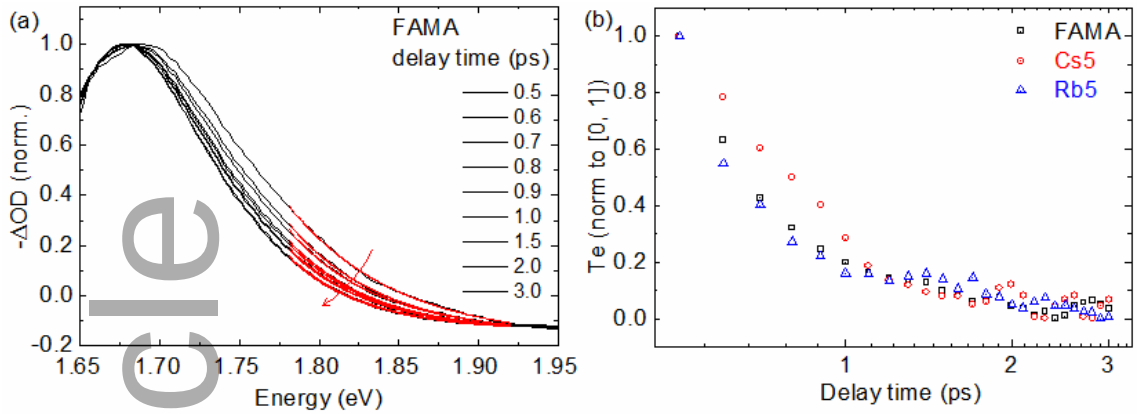

Figure 6. (a) Experimentally measured transient absorption spectra of FAMA films and fits of the high-energy tails to a Maxwell-Boltzmann distribution. For Cs-, Rb-incorporated samples, the respective results can be found in the supporting information. The fiting range is strictly fixed to 1.78 ~ 1.92 eV for all three samples. (b) Normalized hot carrier cooling curves extracted by global fits to the high-energy tails. Here, the initial charge carrier density was 3.5×10^{18} cm^{-3} for all three samples.

Hot-carrier cooling is essentially a multi-step relaxation process in which hot carriers gradually dissipate their excess energy to the crystal lattice by inelastic carrier-phonon interactions.[40] More precisely, it is based on Froehlich interaction between hot carriers and longitudinal phonons (LO) due to the polar nature of the lead-halide perovskites.[22] Following carrier-phonon interaction, LO phonons are converted into low-energy acoustic phonons by the Klemens mechanism, in which one optical phonon is annihilated to create two acoustic phonons with half of the energy and opposite momenta.[41] Finally, the acoustic phonons are transported in the lattice, which completes the cooling process. Hot carrier cooling has previously been studied in perovskites and a model has been proposed earlier by Yang and Price *et al.*[22, 28] This model is based on: i.) a parabolic E~k dependence near the band edge; ii.) a density of states rising with the square root of energy; iii.) photo-excited charges reaching a quasi-equilibrium according to Fermi-Dirac distribution; iv.) bandgap renormalization occurring after excitation, and v.) along with the hot-carrier cooling process, the photo bleaching band gradually moves and finally resembles the steady-state case. Furthermore, recombination losses are neglected on the timescale of carrier cooling, *i.e.*, the population of photo-generated carriers remains unchanged during the cooling process. This model suggests that hot carrier cooling can be monitored at the high-energy tail of transient absorption spectra. Hence, we globally fit the high-energy tails of our TA spectra to extract the effective temperature of hot carriers. The carrier cooling curves are shown in **Figure 6** (b). Note that, to avoid the influence of band gap renormalization,[22, 28] we selected a spectral range from 1.75 - 1.90 eV,

which is at least 100 meV above the band edge. In this range, the distribution of hot carriers can be approximated by the Maxwell-Boltzmann distribution,[22, 28]

$$\Delta OD\ (E) \propto \exp\left(\frac{E_f - E}{k_B T_e}\right) \qquad \textit{Equation 6}$$

where E_f represents Fermi energy, E represents energy, k_B the Boltzmann constant, and T_e the effective charge carrier temperature.

Figure 6 (b) demonstrates that hot carrier cooling in the perovskites studied here is ultrafast and completed on the sub-ps time scale, similar to carrier cooling in $MAPbI_3$ at low charge density.[22, 28] In the present study, the sub-ps cooling process implies strong carrier-phonon coupling in the perovskite film. Surprisingly, the Cs/Rb-cation incorporation does not affect the dynamics of the charge cooling process. As the cooling dynamics are unaffected by Cs/Rb-cation incorporation, we conclude that it has neither an impact on the LO-charge interaction, nor on the decay of LO phonons to acoustic phonons, nor on phonon transport. This is an important finding, which requires theoretical studies to get better insight to the mechanism.

3. Conclusion

In this study, the impact of Cs/Rb-cation incorporation on the photophysics of multiple-cation lead halide perovskites was investigated by a set of steady-state and transient spectroscopy techniques to reveal the origin of device performance differences. We found that upon Cs/Rb incorporation the bandgap and exciton binding energies slightly increase. However, the minor increase in the range of several meV did not affect the devices' short-circuit currents, since the exciton binding energies remained below the thermal energy at room temperature. Similarly, changes of the effective carrier mass determined in the framework of the Burstein-Moss model were found to be in the range of a few tenths of the electron rest mass and thus do not affect the solar cell performance. Furthermore, we studied hot charge carrier cooling and found that the dynamics remained unchanged upon Cs/Rb incorporation. Finally, reduced Urbach energies were measured in Cs/Rb-containing perovskite thin films. From a global fit to the density-dependent carrier recombination dynamics measured by transient absorption spectroscopy, we observed reduced first and retarded second-order charge recombination

upon Cs/Rb incorporation. We conclude that these two factors are the main reasons for the improved device performance observed upon incorporation of small amounts of Cs/Rb and that a trade-off exists in the effect of multiple-cation incorporation in lead mixed halide perovskites, as not all parameters are simultaneously improved.

Supporting Information

Supporting Information is available from the Wiley Online Library or from the author.

Acknowledgement

This publication is based upon work supported by the King Abdullah University of Science and Technology (KAUST) Office of Sponsored Research (OSR) under Award No: OSR-2018-CARF/CCF-3079. Yajun Gao and Kai Wang contributed equally to this work.

References

1. Cho, Kyung Taek; Paek, Sanghyun; Grancini, Giulia; Roldán-Carmona, Cristina; Gao, Peng; Lee, Yonghui; Nazeeruddin, Mohammad Khaja, *Energy & Environmental Science* **2017,** *10* (2), 621-627.

2. Kojima, Akihiro; Teshima, Kenjiro; Shirai, Yasuo; Miyasaka, Tsutomu, *Journal of the American Chemical Society* **2009,** *131* (17), 6050-6051.

3. Snaith, Henry J, *The journal of physical chemistry letters* **2013,** *4* (21), 3623-3630.

4. Yang, Woon Seok; Park, Byung-Wook; Jung, Eui Hyuk; Jeon, Nam Joong; Kim, Young Chan; Lee, Dong Uk; Shin, Seong Sik; Seo, Jangwon; Kim, Eun Kyu; Noh, Jun Hong, *Science* **2017,** *356* (6345), 1376-1379.

5. *NREL Best Research-Cell Efficiency Chart.*

6. Docampo, Pablo; Ball, James M; Darwich, Mariam; Eperon, Giles E; Snaith, Henry J, *Nature communications* **2013,** *4*, 2761.

7. Yang, Dong; Yang, Ruixia; Priya, Shashank; Liu, Shengzhong, *Angewandte Chemie International Edition* **2019,** *58* (14), 4466-4483.

8. Aydin, Erkan; De Bastiani, Michele; Yang, Xinbo; Sajjad, Muhammad; Aljamaan, Faisal; Smirnov, Yury; Hedhili, Mohamed Nejib; Liu, Wenzhu; Allen, Thomas G; Xu, Lujia, *Advanced functional materials* **2019**, 1901741.

9. Bush, Kevin A; Palmstrom, Axel F; Zhengshan, J Yu; Boccard, Mathieu; Cheacharoen, Rongrong; Mailoa, Jonathan P; McMeekin, David P; Hoye, Robert LZ; Bailie, Colin D; Leijtens, Tomas, *Nature Energy* **2017,** *2* (4), 17009.

10. Zhang, Lijun; Liu, Tongfa; Liu, Linfeng; Hu, Min; Yang, Ying; Mei, Anyi; Han, Hongwei, *Journal of Materials Chemistry A* **2015,** *3* (17), 9165-9170.

11. Sha, Wei EI; Ren, Xingang; Chen, Luzhou; Choy, Wallace CH, *Applied Physics Letters* **2015,** *106* (22), 221104.

12. Saliba, Michael; Matsui, Taisuke; Domanski, Konrad; Seo, Ji-Youn; Ummadisingu, Amita; Zakeeruddin, Shaik M.; Correa-Baena, Juan-Pablo; Tress, Wolfgang R.; Abate, Antonio; Hagfeldt, Anders; Grätzel, Michael, *Science (New York, N.Y.)* **2016,** *354* (6309), 206–209.

13. Saliba, Michael; Matsui, Taisuke; Seo, Ji-Youn; Domanski, Konrad; Correa-Baena, Juan-Pablo; Nazeeruddin, Mohammad Khaja; Zakeeruddin, Shaik M; Tress, Wolfgang; Abate, Antonio; Hagfeldt, Anders, *Energy & environmental science* **2016,** *9* (6), 1989-1997.

14. Yi, Chenyi; Luo, Jingshan; Meloni, Simone; Boziki, Ariadni; Ashari-Astani, Negar; Grätzel, Carole; Zakeeruddin, Shaik M; Röthlisberger, Ursula; Grätzel, Michael, *Energy & Environmental Science* **2016,** *9* (2), 656-662.

15. Dang, Hoang X; Wang, Kai; Ghasemi, Masoud; Tang, Ming-Chung; De Bastiani, Michele; Aydin, Erkan; Dauzon, Emilie; Barrit, Dounya; Peng, Jun; Smilgies, Detlef-M, *Joule* **2019**.

16. Wang, Kai; Tang, Ming-Chun; Dang, Hoang X; Munir, Rahim; Barrit, Dounya; De Bastiani, Michele; Aydin, Erkan; Smilgies, Detlef-M; De Wolf, Stefaan; Amassian, Aram, *Advanced Materials* **2019**, 1808357.

17. Hu, Yinghong; Aygüler, Meltem F; Petrus, Michiel L; Bein, Thomas; Docampo, Pablo, *ACS Energy Letters* **2017,** *2* (10), 2212-2218.

18. Hu, Yinghong; Hutter, Eline M; Rieder, Philipp; Grill, Irene; Hanisch, Jonas; Aygüler, Meltem F; Hufnagel, Alexander G; Handloser, Matthias; Bein, Thomas; Hartschuh, Achim, *Advanced Energy Materials* **2018**, 1703057.

19. Liu, Shungshuang; Huang, Wenchao; Liao, Peizhe; Pootrakulchote, Nuttapol; Li, Hao; Lu, Jianfeng; Li, Junpeng; Huang, Feihong; Shai, Xuxia; Zhao, Xiaojuan, *Journal of Materials Chemistry A* **2017,** *5* (44), 22952-22958.

20. Wehrenfennig, Christian; Eperon, Giles E.; Johnston, Michael B.; Snaith, Henry J.; Herz, Laura M., *Advanced Materials* **2014,** *26* (10), 1584–1589.

21. Wehrenfennig, Christian; Liu, Mingzhen; Snaith, Henry J; Johnston, Michael B; Herz, Laura M, *Energy & Environmental Science* **2014,** *7* (7), 2269-2275.

22. Yang, Ye; Ostrowski, David P; France, Ryan M; Zhu, Kai; Van De Lagemaat, Jao; Luther, Joseph M; Beard, Matthew C, *Nature Photonics* **2016,** *10* (1), 53.

23. Yang, Ye; Yan, Yong; Yang, Mengjin; Choi, Sukgeun; Zhu, Kai; Luther, Joseph M; Beard, Matthew C, *Nature communications* **2015,** *6*, 7961.

24. De Wolf, Stefaan; Holovsky, Jakub; Moon, Soo-Jin; Löper, Philipp; Niesen, Bjoern; Ledinsky, Martin; Haug, Franz-Josef; Yum, Jun-Ho; Ballif, Christophe, *The journal of physical chemistry letters* **2014,** *5* (6), 1035-1039.

25. Ledinsky, Martin; Schönfeldová, Tereza; Holovský, Jakub; Aydin, Erkan; Hájková, Zdeňka; Landová, Lucie; Neyková, Neda; Fejfar, Antonín; De Wolf, Stefaan, *The journal of physical chemistry letters* **2019,** *10* (6), 1368-1373.

26. Pathak, Sandeep; Sepe, Alessandro; Sadhanala, Aditya; Deschler, Felix; Haghighirad, Amir; Sakai, Nobuya; Goedel, Karl C; Stranks, Samuel D; Noel, Nakita; Price, Michael, *ACS nano* **2015,** *9* (3), 2311-2320.

27. Xing, Guichuan; Mathews, Nripan; Sun, Shuangyong; Lim, Swee Sien; Lam, Yeng Ming; Grätzel, Michael; Mhaisalkar, Subodh; Sum, Tze Chien, *Science* **2013,** *342* (6156), 344-347.

28. Price, Michael B; Butkus, Justinas; Jellicoe, Tom C; Sadhanala, Aditya; Briane, Anouk; Halpert, Jonathan E; Broch, Katharina; Hodgkiss, Justin M; Friend, Richard H; Deschler, Felix, *Nature communications* **2015,** *6*, 8420.

29. Manser, Joseph S.; Kamat, Prashant V., *Nature Photonics* **2014,** *8* (9), 737.

30. Saliba, Michael; Matsui, Taisuke; Domanski, Konrad; Seo, Ji-Youn; Ummadisingu, Amita; Zakeeruddin, Shaik M; Correa-Baena, Juan-Pablo; Tress, Wolfgang R; Abate, Antonio; Hagfeldt, Anders, *Science* **2016,** *354* (6309), 206-209.

31. Elliott, RJ, *Physical Review* **1957,** *108* (6), 1384.

32. Liu, Dongyan; Li, Shanshan; Bian, Fang; Meng, Xiangying, *Materials* **2018,** *11* (7), 1141.

33. Prasanna, Rohit; Gold-Parker, Aryeh; Leijtens, Tomas; Conings, Bert; Babayigit, Aslihan; Boyen, Hans-Gerd; Toney, Michael F; McGehee, Michael D, *Journal of the American Chemical Society* **2017,** *139* (32), 11117-11124.

34. McCluskey, Matthew D; Haller, Eugene E, *Dopants and defects in semiconductors*. CRC Press: 2012.

35. Adachi, Sadao, *Optical properties of crystalline and amorphous semiconductors: Materials and fundamental principles*. Springer Science & Business Media: 2012.

36. Johnston, Michael B; Herz, Laura M, *Accounts of chemical research* **2015,** *49* (1), 146-154.

37. Meggiolaro, Daniele; De Angelis, Filippo, *ACS Energy Letters* **2018,** *3* (9), 2206-2222.

38. Crothers, Timothy W; Milot, Rebecca L; Patel, Jay B; Parrott, Elizabeth S; Schlipf, Johannes; Müller-Buschbaum, Peter; Johnston, Michael B; Herz, Laura M, *Nano letters* **2017,** *17* (9), 5782-5789.

39. Yang, Ye; Gu, Jing; Young, James L.; Miller, Elisa M.; Turner, John A.; Neale, Nathan R.; Beard, Matthew C., *Science (New York, N.Y.)* **2015,** *350* (6264), 1061–1065.

40. Nozik, Arthur J; Conibeer, Gavin; Beard, Matthew C, *Advanced concepts in photovoltaics*. Royal Society of Chemistry: 2014.

41. Fox, Mark, Optical properties of solids. Oxford University Press: 2002.

Short Summary for TOC

The partial substitution of methylammonium (MA) and formamidinium (FA) cations by cesium (Cs) or rubidium (Rb) cations in multiple-cation lead mixed halide perovskites, ($FA_{0.83}MA_{0.17}Pb(I_{0.83}Br_{0.17})_3$), reduces the trap-assisted (k_1) and radiative (k_2) charge carrier recombination rate. Furthermore, Urbach energies are reduced, indicating improved perovskite film microstructure. Consequently, photovoltaic devices with Cs/Rb-incorporated perovskites exhibit improved power conversion efficiency.